



HAL
open science

Airborne observations of fast-evolving ocean submesoscale turbulence

Hector S. Torres, Ernesto Rodriguez, Alexander Wineteer, Patrice Klein, Andrew F. Thompson, Jörn Callies, Eric d'Asaro, Dragana Perkovic-Martin, J. Thomas Farrar, Federica Polverari, et al.

► **To cite this version:**

Hector S. Torres, Ernesto Rodriguez, Alexander Wineteer, Patrice Klein, Andrew F. Thompson, et al.. Airborne observations of fast-evolving ocean submesoscale turbulence. *Communications Earth & Environment*, 2024, 5, 10.1038/s43247-024-01917-3 . insu-04879851

HAL Id: insu-04879851

<https://insu.hal.science/insu-04879851v1>

Submitted on 10 Jan 2025

HAL is a multi-disciplinary open access archive for the deposit and dissemination of scientific research documents, whether they are published or not. The documents may come from teaching and research institutions in France or abroad, or from public or private research centers.

L'archive ouverte pluridisciplinaire **HAL**, est destinée au dépôt et à la diffusion de documents scientifiques de niveau recherche, publiés ou non, émanant des établissements d'enseignement et de recherche français ou étrangers, des laboratoires publics ou privés.



Distributed under a Creative Commons Attribution 4.0 International License

<https://doi.org/10.1038/s43247-024-01917-3>

Airborne observations of fast-evolving ocean submesoscale turbulence

Check for updates

Hector S. Torres¹✉, Ernesto Rodriguez¹, Alexander Wineteer¹, Patrice Klein^{1,2,3}, Andrew F. Thompson², Jörn Callies², Eric D'Asaro⁴, Dragana Perkovic-Martin¹, J. Thomas Farrar⁵, Federica Polverari¹ & Ruzbeh Akbar¹

Ocean images collected by astronauts onboard the Apollo spacecraft more than 50 years ago revealed a large number of ocean eddies, with a size between 1 and 20 km. Since then, satellite infrared, ocean color, sun glitter and synthetic aperture radar images, with high spatial resolution, have confirmed the ubiquitous presence of these small eddies in all oceans. However, observing the dynamical characteristics and evolution of these eddies has remained challenging. An experiment was recently carried out in the California Current system using the new airborne Doppler Scatterometer (National Aeronautics and Space Administration-Jet Propulsion Laboratory DopplerScatt) instrument that observes surface velocities. Here, with DopplerScatt, we mapped a 30 × 100 km domain over multiple days to unveil numerous 1–20 km ocean eddies, called submesoscale eddies, that evolve over a period of a few hours. The strong interactions between eddies generate horizontal velocity divergence, implying vertical velocities reaching 250 m day⁻¹ at 40 m depth. The velocity field also produces horizontal dispersion of particles over a distance of 50 km within 12 h, which rapidly fills the turbulent eddy field. These observations suggest that submesoscale ocean turbulence may profoundly affect the vertical transport of heat, carbon, and important climatic gases between the atmosphere and the ocean interior, as well as the horizontal dispersion of tracers and particles. As such, submesoscale ocean eddies are a critical element of Earth's climate system.

In 2000, Walter Munk¹ analyzed more than 500 photographs collected by astronauts on board the Apollo and Space Shuttle missions. These photographs are sun glitter images (reflectance of the sun on the sea surface) that revealed a high density of interconnected eddies with a diameter ranging from 1 to 20 km (Fig. 1a). Estimation of the sharp break of ships' wakes present on these images indicated that the velocity associated with these eddies can reach 0.2 m s⁻¹ and a horizontal shear of 10⁻³ s⁻¹. Since then, the ubiquitous existence of such interconnected, small-scale eddies, which Paul Sculler-Power (the only astronaut oceanographer) called in 1986 submesoscale eddies, has been confirmed by satellite infrared, ocean color, sun glitter, and synthetic aperture radar images. A recent study based on ocean color satellite images emphasizes that these cyclonic and anticyclonic submesoscale eddies are present in all seasons with a slight predominance of cyclonic eddies². Several mechanisms have been proposed to explain the emergence of these submesoscale eddies, such as gravity convection, horizontal current shear, mixed-layer instabilities, wind

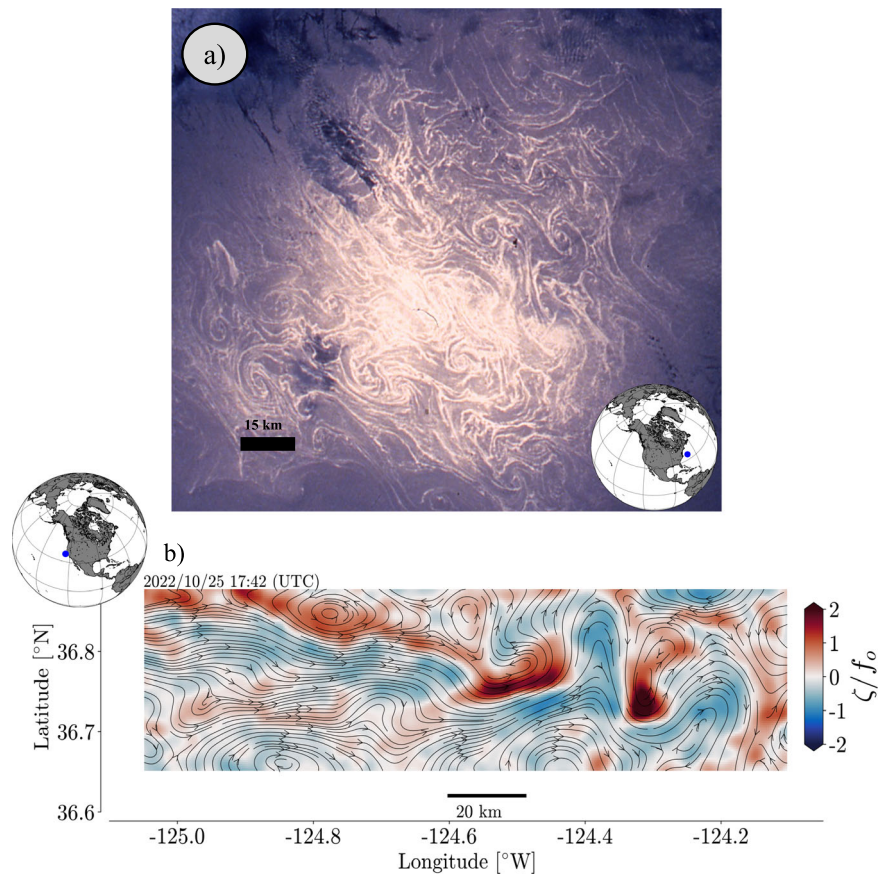
intermittency, and frontal instability^{3–9}, all of which are relevant for the upper ocean¹⁰.

The magnitudes of the horizontal velocities and horizontal shears estimated by ref. 1 have been confirmed by a few recent in situ experiments focusing on isolated eddies^{3,6}. Recent studies^{11–13} suggest these large values of velocities and shears may result from the mutual interactions between eddies, leading to a vigorous vertical circulation in the upper oceanic layers that connects the ocean interior to the atmosphere. It has remained challenging so far, however, to assess the processes underlying the submesoscale interactions and the resulting vertical circulation from in situ observations, because the rapidly evolving circulation requires observations spanning a wide range of spatial scales that can evolve over a period of a day.

Here we report on progress toward meeting this challenge using an airborne Doppler Scatterometer instrument (NASA-JPL DopplerScatt)¹⁴ deployed during the 2022 S-MODE campaign¹⁵ (Fig. 19Sb–e). DopplerScatt

¹Jet Propulsion Laboratory, California Institute of Technology, Pasadena, CA, USA. ²Department of Environmental Science and Engineering, California Institute of Technology, Pasadena, CA, USA. ³Laboratoire de Météorologie Dynamique, Ecole Normale Supérieure, Paris, France. ⁴Applied Physics Laboratory, University of Washington, Seattle, WA, USA. ⁵Woods Hole Oceanographic Institution, Woods Hole, MA, USA. ✉e-mail: hector.torres.gutierrez@jpl.nasa.gov

Fig. 1 | A view of the ocean turbulence from space and from airborne observations. a Photograph taken off the northeastern seaboard of the United States in October 1984 during the Space Shuttle mission STS-41G¹. The photo shows spiral eddies in the Gulf Stream highlighted in the Sun glitter. **b** DopplerScatt relative vorticity (shading) in the S-MODE area in the California Current System. Black contours are streamlines of the rotational component of the high-pass surface velocity field.



measured the ocean surface velocity over a 30×100 km domain with a spatial resolution of 200 m (see section “Methods”) and an accuracy better than $.04 \text{ m s}^{-1}$ over a period of less than 3 h. These observations reveal multiple submesoscale eddies embedded in a mesoscale eddy field, as shown in Figs. 1b and 2, consisting of numerous submesoscale cyclones and anticyclones. The submesoscale eddies evolve over time scales less than 12 h, each one having vorticity (the spin of the eddies) and divergence (associated with vertical velocity) of order $f = 10 \times 10^{-5} \text{ s}^{-1}$, the local planetary vorticity (Fig. 19S). We analyze a subset of the DopplerScatt data to characterize the eddy interactions and their relationship with divergence and horizontal dispersion.

Results

Submesoscale eddies between two mesoscale eddies

The domain mapped by DopplerScatt between October 24 and 26 (black rectangle in Fig. 19Sc) is located between a cold cyclonic eddy centered at 37°N , 124.5°W (‘C’ in Fig. 19Sc) and a warm anticyclonic eddy at 36°N , 126°W (‘A’ in Fig. 19Sc). Both mesoscale eddies have a diameter of ~ 150 km and horizontal geostrophic velocities of $\sim 0.3\text{--}0.4 \text{ m s}^{-1}$. These mesoscale eddies were identified from satellite altimetry and remained nearly stationary during the three days. A cloud-free sea surface temperature (SST) satellite image was available only on the last day (Fig. 19Sc,d), displaying a roughly zonal SST front between the two mesoscale eddies with a temperature gradient reaching $0.5 \text{ }^\circ\text{C km}^{-1}$ (Fig. 19Sd). Each day, DopplerScatt observations revealed the presence of about 20 submesoscale eddies in the 30×100 km domain, with their diameters ranging from 2 km up to 20 km (Fig. 1b). These eddies are found on both sides of an eastward zonal flow roughly located around a latitude of 36.8°N . The SST satellite image on October 26 suggests this zonal flow is related to the SST front. Figure 2 emphasizes that the submesoscale eddies evolve from one day to the other and even within 6 h (Fig. 3).

Dynamics of the submesoscale eddies are also reflected in the statistics of their associated velocity gradients, such as vorticity, strain, and divergence (see section “Methods”), which were calculated after smoothing the DopplerScatt velocities using a Gaussian spatial filter with a full width half maximum of 2 km (Fig. 4). Vorticity, strain and divergence at this scale have an RMS value of order f . The vorticity reaches a maximum close to $4f$, whereas negative values have a much smaller magnitude. This skewness (1.27 here) has been observed previously in some ship-based surveys^{3,16,17}. Divergence is slightly negatively skewed, with an RMS value somewhat less than vorticity. Assuming the divergence is uniform in the upper half of the mixed-layer leads to vertical velocities with maxima of 250 m day^{-1} at a depth of 40 m and an RMS value of 75 m day^{-1} , a value two times larger than estimated in numerical models with a spatial resolution of 500 m ¹⁸.

Figure 2 and Fig. 20S further reveal that the submesoscale patterns of vorticity, strain, and divergence exhibit conspicuous dipole structures in between eddies over three consecutive days (white lines in Fig. 2), with the vorticity patterns anticorrelated with divergence patterns (see also Fig. 23Sa). This suggests that the divergence field, and therefore the vertical velocity field associated with submesoscale eddies, is enhanced by the interactions between cyclonic and anticyclonic eddies.

The DopplerScatt velocities show kinetic energy distributed over a wide range of scales (Fig. 4c), as characteristic of strongly nonlinear turbulent flows. The kinetic energy spectrum approximately follows a power law k^{-2} between 2 and 40 km with k the wavenumber, which is consistent with numerical studies^{19–23} and in situ observations²⁴ of energetic submesoscale turbulence. Furthermore, a power law k^{-2} indicates that while smaller-scale eddies have less kinetic energy than larger-scale eddies, velocity gradients are dominated by the submesoscale eddies²⁵. Roughly, the RMS values of divergence and vorticity at 2 km are ten times as large as they are at 200 km (see section “Methods” and Fig. 4d), indicating a shift in dynamics between mesoscale and submesoscale eddies.

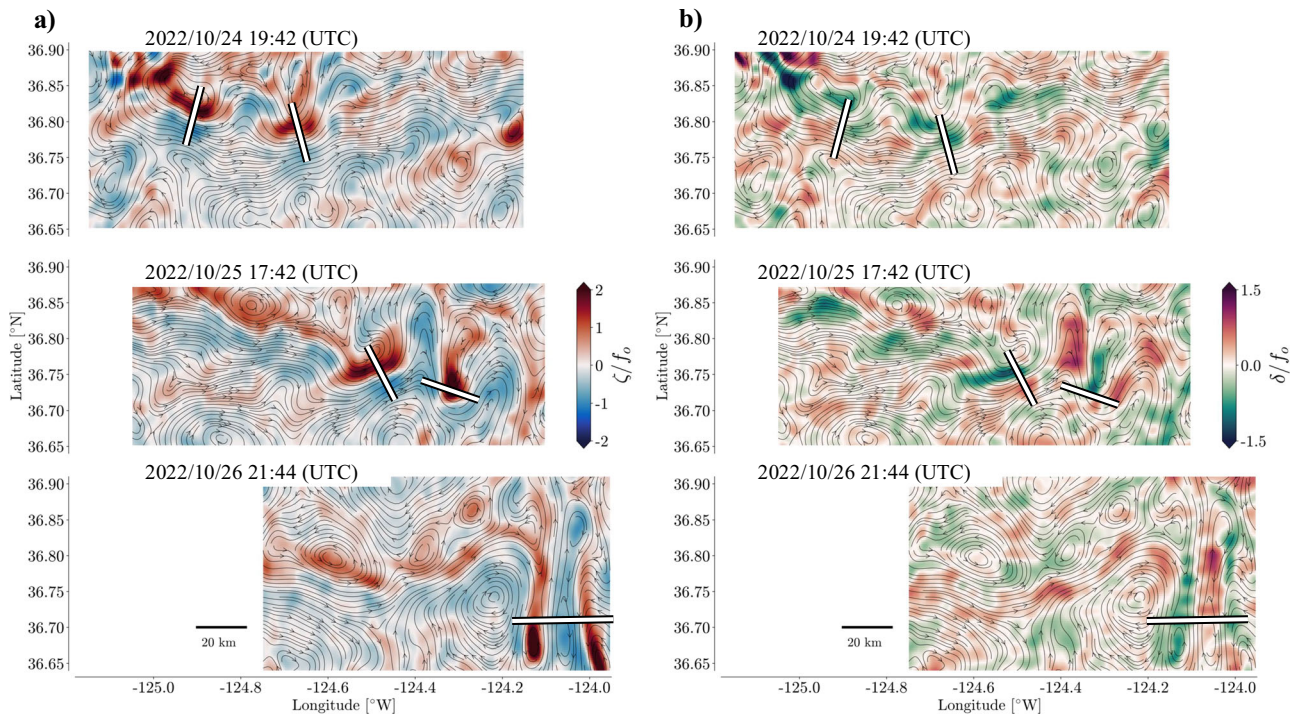


Fig. 2 | Evolution of submesoscale field. Daily evolution of surface vorticity (a) and divergence (b) computed at 2-km scale from DopplerScatt observations over three consecutive days. These times represent the average time of each map. Each map took ~3 h to form. Black contours are streamlines of the rotational component of the

high-pass surface velocity field (see section “Methods”). Shading shows the vorticity (a) and divergence (b) normalized by the Coriolis frequency f , corresponding to a period of about 20 h. The white lines mark the location of dipole structures.

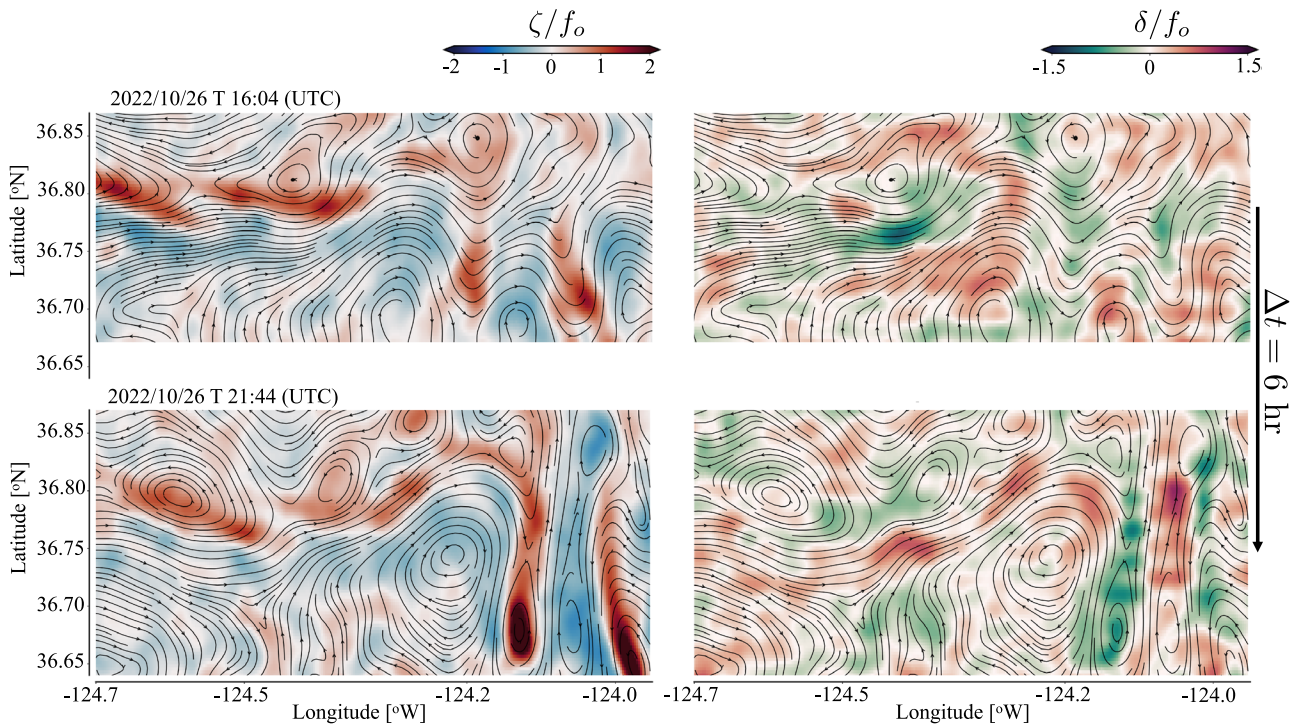
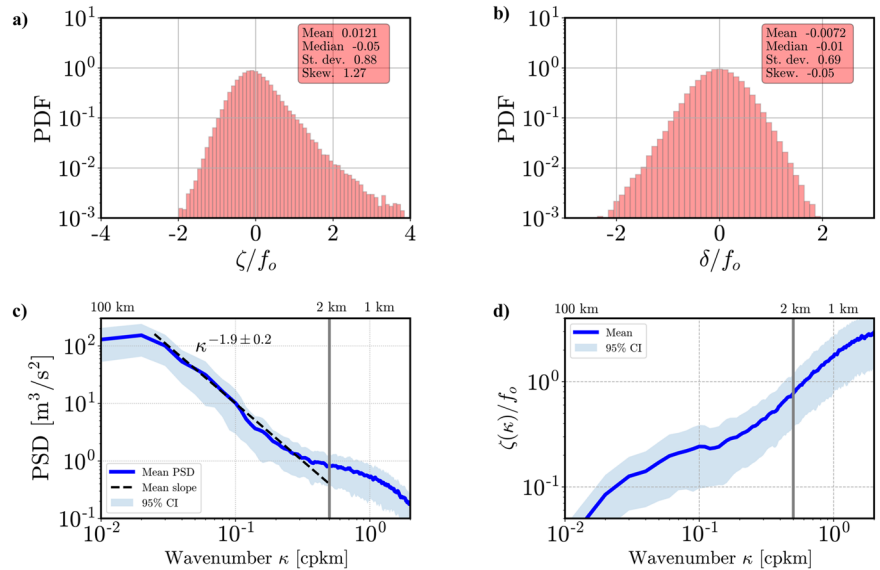


Fig. 3 | Fast-evolving of surface vorticity and divergence computed at 2-km scale from DopplerScatt observations on October 26th, 2022 at 16:04 UTC (top panels) and 21:44 UTC (bottom panels). These times represent the average time of each map. Each map took ~3 h to form. Black contours are streamlines of the

rotational component of the high-pass surface velocity field (see section “Methods”). Shading shows the vorticity (left panels) and divergence (right panels) normalized by the Coriolis frequency, f , corresponding to a period of about 20 h.

Fig. 4 | Statistics of submesoscale motions. Probability density histograms of surface relative vorticity (a), divergence (b) normalized by the Coriolis frequency f_o . Velocity gradients were computed from DopplerScatt observations smoothed to 2 km. c Power spectral density for unfiltered DopplerScatt surface currents. The spectrum was computed avoiding the edges of the swath (see Section 4 in SI for more information). The mean spectral slope between in the 2–40 km wavelength range is in $\kappa^{-1.9 \pm 0.2}$ computed from least-square fitting. d Spectrum of vorticity normalized by f_o . The shaded region represents the 95% confidence interval from the mean spectrum based on the spread of spectral realizations across flights.



The dynamical balance of submesoscale eddies diverge from the mesoscale

The strong curvature and large velocity gradients associated with submesoscale eddies (Fig. 1b) suggest these eddies may be affected by centripetal forces and therefore are not in geostrophic balance. Geostrophic balance occurs when the Coriolis forces, $fz \times u$, almost balance the pressure gradients, $\nabla p/\rho$, in the momentum equation,

$$\frac{d\mathbf{u}}{dt} + fz \times \mathbf{u} = -\frac{\nabla p}{\rho}, \tag{1}$$

where \mathbf{u} is the velocity, \mathbf{z} is a unit vector pointing up, p is pressure, and ρ is density. Indeed, such strong curvature usually supplies an additional inward centripetal force, included in the acceleration of fluid parcels, $d\mathbf{u}/dt$, causing submesoscale eddies to evolve much faster than mesoscale eddies, which are associated with weaker curvature²⁶.

We quantify the departure of submesoscale eddies from geostrophic balance through the analysis of the horizontal divergence of the momentum equation (1) (see section “Methods”). Maps of the divergence of the accelerations (Fig. 5a) and of the divergence of the Coriolis term (Fig. 5b) indicate that both contributions have similar magnitudes. The divergence of the accelerations is largest between eddies, which emphasizes the impact of Lagrangian accelerations on eddy interactions as found in numerical studies^{27,28}. A substantial departure from geostrophic balance occurs, as expected, where the Rossby number is large (Fig. 5d). In addition, when the explicit contribution of the divergence (δ) is not taken into account in Eq. (5) (see section “Methods”), the departure from geostrophy is weaker: the differences between Fig. 5d, e highlight the impact of δ in the momentum balance of submesoscale eddies.

Lagrangian accelerations, $d\mathbf{u}/dt$, also impact the dispersion of particles and tracers, leading them to move around eddies and ultimately fill the whole eddy field^{29,30}. The key quantities involved in the dispersion mechanisms are the strain, σ , relative vorticity, ζ , and divergence, δ (see section “Methods”). We have estimated the dispersion of particles and tracers embedded in the submesoscale eddy field using the Okubo-Weiss quantity³⁰ (involving the strain and vorticity fields) diagnosed from DopplerScatt observations (see Eqs. 8 and 9 in section “Methods”, and Fig. 21S). The separation distance between two particles increases from 1 km to 50 km in just 12 h. The same increase takes more than 20 days if only the mesoscale eddy field observed by altimeter products is present. This highlights the strong efficiency of submesoscale eddies to quickly disperse any tracers and particles.

These results indicate that the large magnitude of the Lagrangian accelerations associated with the strong curvature of submesoscale eddies explains the fast interactions between these eddies within a few hours, compared with the slow time evolution of mesoscale eddies. They further emphasize the strong relationship between submesoscale eddy interactions and divergence.

Submesoscale interactions and divergence

Eddy interactions are usually assessed through KE transfer between scales. We have estimated the cross-scale KE transfer associated with submesoscales using a coarse-graining approach that estimates the KE transfer between large (>5 km) and small (<5 km) scales^{31,32} (“Methods”). Similar results are obtained if the threshold is set to larger (7 km) or smaller scales (3 km) than 5 km. The cross-scale KE transfer magnitude is largest in between submesoscale eddies (Fig. 6a). These transfers can be either positive or negative, with their magnitudes of the order of $2 \times 10^{-7} \text{ m}^2 \text{ s}^{-3}$, which corresponds to a KE change of about $.004 \text{ m}^2 \text{ s}^{-2}$ within 6 h. The KE of scales smaller than 5 km has a magnitude of up to $0.01 \text{ m}^2 \text{ s}^{-3}$ and is located in the same regions as the KE transfers, i.e., in-between submesoscale eddies (Fig. 6b). This indicates that the KE at small scales can increase or decrease by a factor of about two at the expense or benefit of larger scales within a few hours. These observational results are remarkably similar to those from a recent numerical study by Srinivasan et al.³² in the Northeast Atlantic, not only in terms of the location of KE at small scales and KE transfer with respect to submesoscale eddies but also in terms of the order of magnitude of these quantities.

Scale transfers of KE are governed by the strain and divergence of larger scales (see Eq. (11) in “Methods” and Fig. 23bSI). For divergent flows, KE transfers can go to either small or large scales, whereas purely rotational flows tend only to transfer energy to larger scales^{11,13,33,34}. Here, we analyze the specific contribution of the divergence to these KE transfers. DopplerScatt measurements from four consecutive flights reveal that in-between submesoscale eddies, there is a dipole of divergence anticorrelated with KE transfer (white lines in Figs. 2 and Fig. 22SI). On average, KE transfers have the opposite sign as divergence (Fig. 6c, see also Fig. 23bSI), emphasizing the relationship between divergence and submesoscale interactions. This finding is complementary to the importance of the shear strain in the downscale KE fluxes across a cold filament reported in¹³.

The four flights are insufficient to conclude whether submesoscale eddies contribute to the net transfer energy to large scales, leading to strengthened mesoscale eddies, or to small scales, leading to KE dissipation. The KE transfers from four flights produce an average transfer

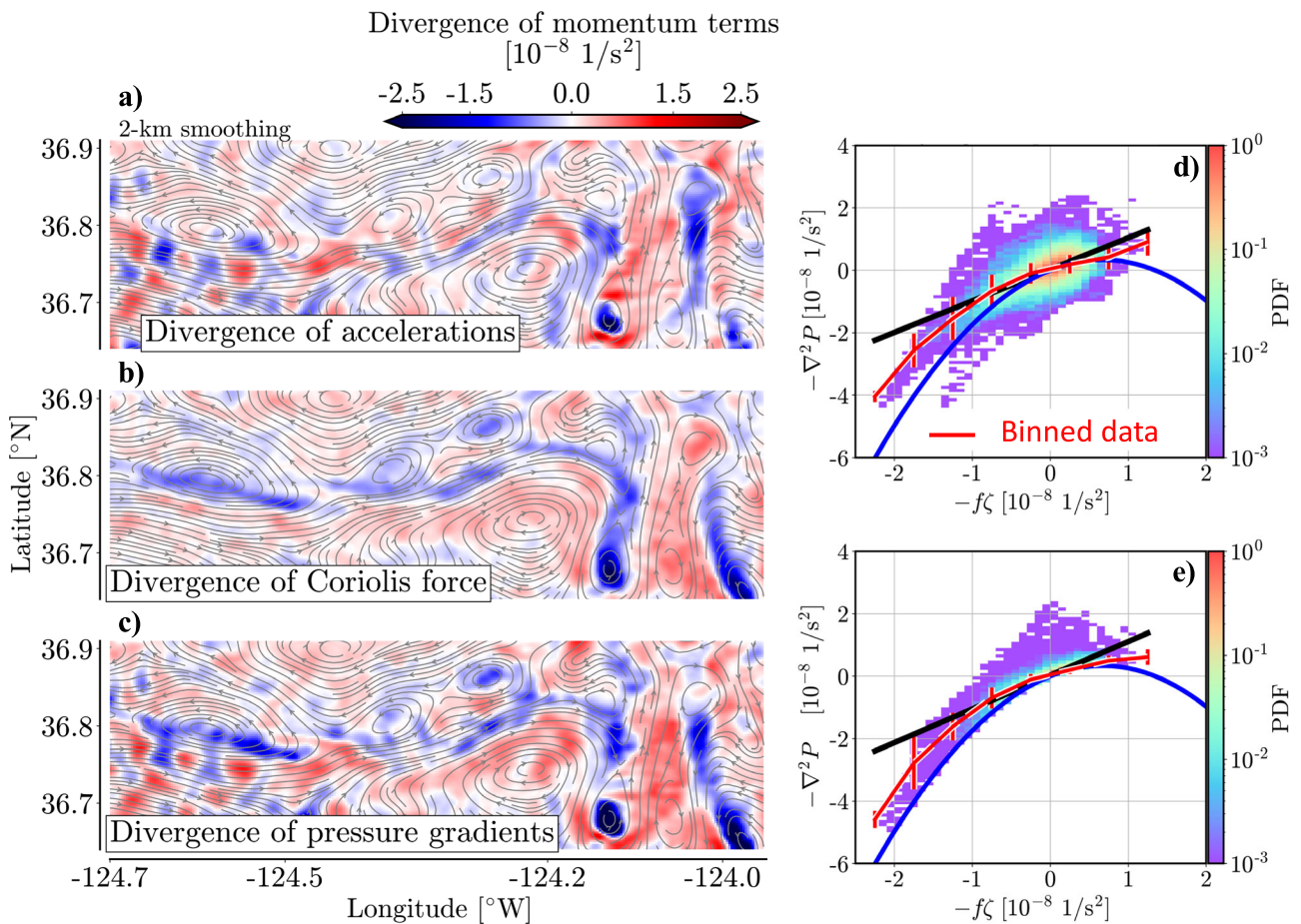


Fig. 5 | Dynamical balance. **a** Divergence of accelerations, **b** divergence of Coriolis forces, and **c** divergence of pressure gradients estimated from the divergence budget (Eq. (5)) (see section “Methods”). The maps in (a–c) corresponds to October 26th, 2022 at 21:44 UTC. **d** Scatterplot between the divergence of pressure gradients and divergence of Coriolis forces. The solid black line represents a balance between the divergence of pressure gradients and divergence of Coriolis forces, or geostrophic

balance. **e** The same as (d) except that the pressure Laplacian is estimated from Eq. (5) without considering δ . The blue curve is an approximation of the ageostrophic balance ($-\nabla^2 P_{ag} = -\frac{\zeta}{2} - f\zeta$). Four consecutive DopplerScatt flights (from October 24 to October 26) were used to construct the scatterplots. The uncertainty in the estimation of the divergence of pressure gradients is smaller than 40% of f^2 at 2-km scale (see SI Section 6).

$6.0 \pm 2.2 \times 10^{-9} \text{ m}^2 \text{ s}^{-3}$ (95 % CI Jackknife estimate, 480 DOF) to small scales. However, this estimates are associated to a particular mesoscale-induced frontogenesis observed during four days, more flights or a bigger domain are needed to accumulate sufficient statistics for a robust estimate of the net transfer.

Summary and discussion

DopplerScatt measurements reveal a large number of interconnected sub-mesoscale eddies evolving over a period of a few hours. These observations provide direct evidence that cross-scale interactions, over a scale range from 1 km down to 100 km, lead to large horizontal divergence at submesoscales and vertical velocities reaching 250 m day^{-1} at a depth of 40 m. These results emphasize that cross-scale interactions may profoundly affect the vertical transport of heat, carbon, and important climatic gases, as well as the horizontal dispersion of tracers and particles, which emphasizes the need to consider these unresolved interactions in climate models.

A caveat must be mentioned regarding the amplitude of the velocity gradients reported here. The filter level of 2-km has been chosen to avoid noise associated with DopplerScatt sampling (Section 4 in SI). However, the large magnitudes of velocity gradients associated with submesoscale eddies can vary significantly if the smoothing level slightly increases or decreases. Indeed, for a velocity spectrum slope in $k^{-5/3}$, velocity gradients are proportional to $k^{2/3}$ (see section “Method” 6.6). This means that according to this spectral argument, the divergence δ at 1 km (10 km) is larger (smaller) than the divergence at 2 km by a factor of 1.6 (4.6), and therefore the vertical

velocity field. But, we can only estimate velocity gradients, and therefore vertical velocity, for scales larger than or equal to 2 km with the present DopplerScatt data.

The DopplerScatt velocity fields highlight the existence of many dipole structures in between eddies that characterize their interactions. The anticorrelation between vorticity and divergence within these dipoles is suggestive of the relationships predicted by frontogenesis theory³⁵: cyclonic vorticity tends to be associated with surface convergence ($\delta < 0$) and thus downwelling (usually found in the cold side of a front), whereas anticyclonic vorticity tends to be associated with divergence ($\delta > 0$) and thus upwelling (warm side of a front).

Important questions remain related to the interactions between mesoscales and submesoscales: (i) what instabilities (shear instability, convective instability, frontal or mixed-layer instabilities) energize sub-mesoscale eddies and (ii) what is the net direction and strength of the KE transfer between scales over larger scales. Addressing these questions would require observations of submesoscale turbulence over a domain large enough to capture a full mesoscale/submesoscale eddy field, such as a $200 \text{ km} \times 200 \text{ km}$ domain, as well as persistent access to high-resolution SST images.

We have compared our results with those from a numerical model with a spacing grid resolution of 500 m, configured for the CCS region during the same season as the S-Mode experiment. Statistics for the vorticity, divergence and Okubo–Weiss quantity from numerical outputs, spatially smoothed to 2-km as the DopplerScatt observations, reveal RMS values that

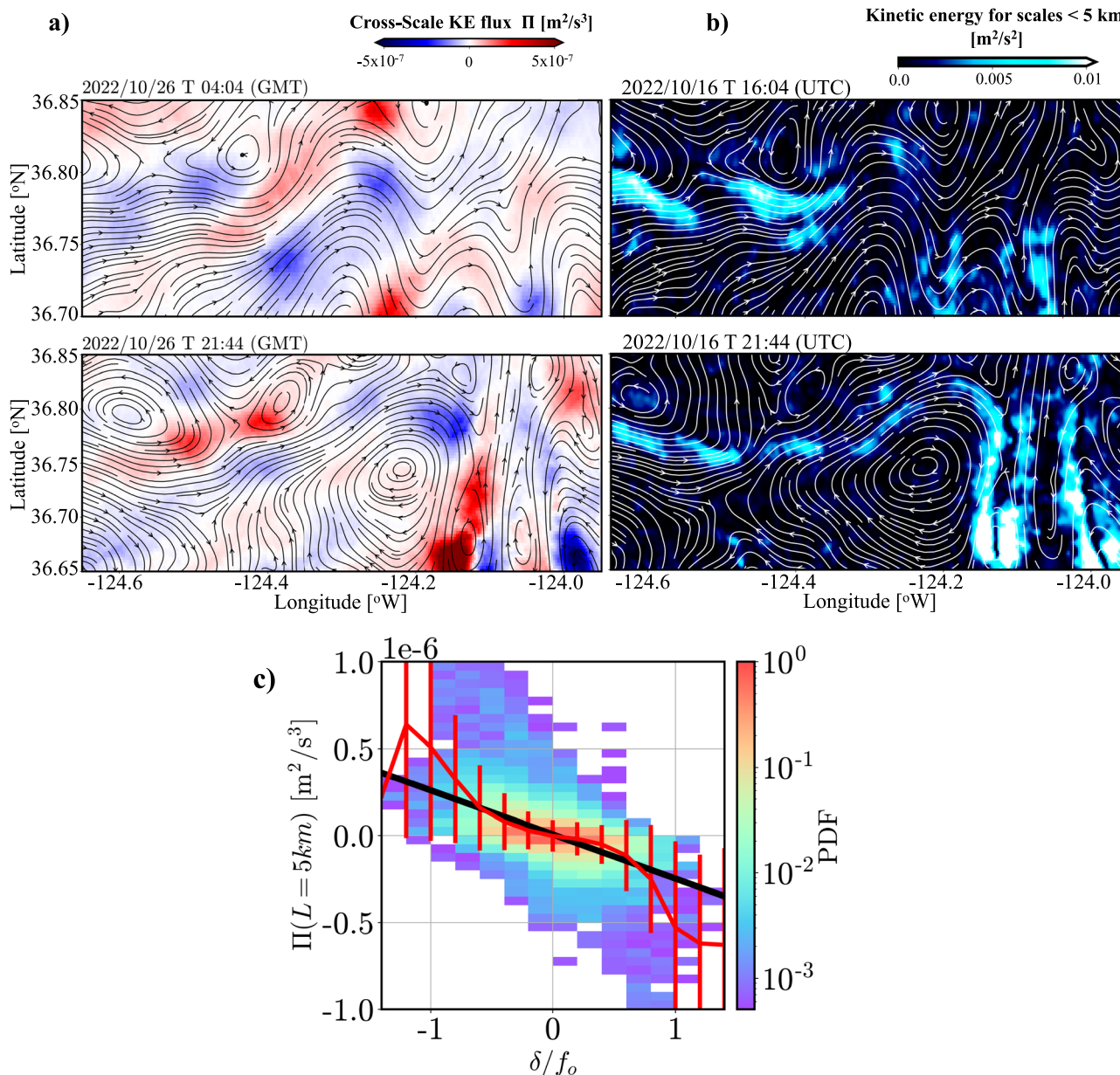


Fig. 6 | Cross-scale submesoscale interactions. **a** Surface cross-scale kinetic energy flux (Π) through 5 km scales, computed with a coarse-graining approach: Red (blue) color represents kinetic energy flux from larger (smaller) scales to smaller (larger) scales relative to 5 km. **b** Surface kinetic energy for scales smaller than 5 km. **c** Relationship between divergence (δ) and cross-scale kinetic energy flux (Π) using the four flights.

are 2.5 times smaller than those diagnosed from observations (Figs. 24SI and 25SI). Furthermore, the modeled submesoscale structures exhibit principally elongated patterns that differ from the dipole structures revealed by DopplerScatt observations. These differences question the pertinence of existing numerical models to fully reproduce submesoscale dynamics and, in particular, what mechanisms need to be included in these models.

Methods

Sub-mesoscale ocean dynamics experiment (S-MODE)

The S-MODE project is a NASA Earth Ventures Suborbital Investigation designated to test the hypothesis that kilometer-scale ocean eddies make important contributions to the vertical exchange of climate and biological variables in the upper ocean¹⁵. A full description of the S-MODE project can be found in S-MODE. The most novel aspect of S-MODE is the deployment of airborne instruments, in particular the DopplerScatt instrument whose observations collected in October 2022 are the scope of this study.

Satellite altimetry and geostrophic approximation

The background mesoscale eddy field present in the S-Mode domain (126.5–122°W, 35.5–39°N) has been inferred from the sea surface height (SSH) provided by the Near-Real-Time gridded SSALTO/DUACS SSH L4 product <http://marine.copernicus.eu>. Based on Ballarta et al.³⁶, the effective spatial resolution of the gridded anomalies is approximately 150 km in wavelength. SSH is composed of the mean dynamic topography³⁷ and the sea level anomaly maps produced by the DUACS (data unification and altimeter combination system) processing that merges the multi-altimeter along-track constellation. Mesoscale velocities have been diagnosed from SSH using the geostrophic approximation, as follows:

$$\mathbf{z} \times \mathbf{u} = -\frac{g}{f} * \nabla SSH, \quad (2)$$

with \mathbf{z} the vertical unit vector, \mathbf{u} the velocity vector, f the Coriolis frequency, and g the gravitational constant.

Satellite Infrared Image

The Sea Surface Temperature (SST) has been estimated from satellite infrared images provided by Group for High-Resolution Sea Surface Temperature (GHRSSST) and the National Oceanic and Atmospheric Administration (NOAA) <http://www.ghrsst.org>. L2P SST fields were used, as measured by Visible Infrared Imaging Radiometer Suite (VIIRS) instrument, at a spatial resolution of 0.0067°. For a quick access to SST collection covering S-MODE experiments, a catalog of satellite SST images are stored in the following link <http://smode.whoi.edu/satellite/>.

Surface velocities from NASA-JPL DopplerScatt observations

This paper focuses on novel airborne ocean surface velocities carried out by the NASA-JPL Doppler Scatterometer (DopplerScatt) instrument^{14,38,39}, flying on a NASA King Air B200 aircraft.

DopplerScatt is a radar operating at Ka-band. It provides simultaneous measurements of 10-m height ocean surface equivalent neutral winds and vector surface currents tuned to a 4 m depth. The Ka-band signal propagates through clouds, making the system unconstrained by clear weather requirements. However, this is not the case during rain events where DopplerScatt signal could be contaminated. DopplerScatt operated only during free-rain conditions during S-MODE in October 2022.

DopplerScatt is capable of mapping out two-dimensional swaths in latitude-longitude with dimensions of 100 km along-track and 25 km across-track, at a cruise velocity of 250 knots and an altitude of 28,000 feet. The single swaths were covered in ~15 min. A total of 12 single swaths were performed per flight, with an overlapping of 70%. This allows the coverage of the area sketched in Fig. 19Sd,e in 3 h. It is worth noting that 15 min per single-swath permit to capture the fast-evolving nature of the submesoscale eddies reported in this study (see Fig. 2S). Finally, the ground processing of multiple passes allow to reduce the random errors by leveraging the partial overlapping of the footprint. The pixel resolution achieved is 200 m with a random noise level $<O(0.04 \text{ m s}^{-1})$. The principles of measurement and validation of DopplerScatt were described in the context of a field campaign in the Gulf of Mexico^{14,38,39}.

A sensitivity test was performed to determine the best smoothing level that smooths out instrumental noise and the potential noise associated with the DopplerScatt sampling strategy, but retaining as much as possible the characteristics of submesoscale motions. At first glance, the power spectrum density of surface currents and relative vorticity in Fig. 4 do not show a noise floor at high wavenumbers, indicating no instrumental noise. Note that the spectrum was computed avoiding the edges of the swath. In SI Section 4, a detailed analysis of the horizontal maps of relative vorticity and surface divergence, and their respective statistics is reported. It is demonstrated that surface divergence suffers more due to the orientation of the swaths, east-west orientation in this particular experiment. In particular, the across-track velocity component (north-south velocity component) displays large noise at the edges of the swath. This noise is visually detected as stripes along swaths. The overlapping of swaths during flights is not sufficient to reduce the noise, so additional smoothing must be applied to get rid of these strips. A 2-km smoothing level is sufficient to get rid of them, and it is sufficient to characterize the submesoscale turbulence observed by DopplerScatt.

An estimation of the error of diagnosed velocity gradients has been done (see SI part). The velocity gradients were calculated using a centered difference scheme. The error associated to the velocity gradients computed using the unsmoothed velocities can be as large as f_0 , with $f_0 = 0.8 \times 10^{-4} \text{ s}^{-1}$. However, a Gaussian spatial filter were used to reduce the noise in the velocity gradients, with an e-folding scale $L_G (L_G = (L/2.3548)/\text{pixel}_{\text{size}})$, where L is the spatial averaging scale associate to the full width half maximum of the Gaussian smoother, and $\text{pixel}_{\text{size}} = 200 \text{ m}$ (see SI). Using a Gaussian filter with a full width half maximum of 2 km, the error reaches $0.15f_0$ at the center of the domain and $0.3f_0$ at the edges of the domain (see SI).

Velocity power spectral density

A multitaper spectral analysis was performed on a 100 km slices along DopplerScatt flight tracks to estimate power spectral density of ocean

surface currents. About 200 independent spectral realizations per flight were averaged together to reduce noise. DopplerScatt currents were interpolated onto a regular grid using a cubic spline interpolation with a spacing of 200 m. The spectral slope and its standard error was estimated using least-square fitting.

DopplerScatt velocities are characterized by a KE spectral slope close to k^{-2} between 2 km and 40 km with k the wavenumber (Fig. 4d). From these spectral characteristics, smaller eddies have smaller KE than larger eddies but larger velocity gradients. Indeed, the variance of the velocity gradient can be expressed in terms of $k^{25,40}$ as $[k^3 KE(k)]^{1/2}$, with $KE(k)$ the power spectral density of the kinetic energy at wavenumber k , with units of $\text{m}^3 \text{ s}^{-2}$. Note that the contribution of an eddy to the wavenumber slope of the spectrum in log-log is not the same as its contribution to the variance as a function of wavenumber. Thus, for a $k^{-5/3}$ spectrum slope, velocity gradients are proportional to $k^{2/3}$. This means that an eddy with a diameter of 2 km will have velocity gradients about 10 times larger than those for an eddy with a diameter of 200 km (Fig. 5d). Since large velocity gradients are expected at small scales, KE at small scales should be found where large velocity gradients are located, i.e., in-between submesoscale eddies. The implications of this result are discussed below.

Diagnosing Lagrangian accelerations

The time evolution of surface velocities is driven by pressure forces through the momentum equations:

$$\frac{d\mathbf{u}}{dt} + f\mathbf{z} \times \mathbf{u} = -\nabla P, \quad (3)$$

with P the pressure. The geostrophic balance implies that pressure gradients are balanced by the Coriolis forces, i.e.,

$$f\mathbf{z} \times \mathbf{u} \approx -\nabla P, \quad (4)$$

and therefore that the acceleration terms, $\frac{d\mathbf{u}}{dt}$ are much smaller than the Coriolis forces.

To infer the dynamical balance of submesoscale eddies, we have considered the divergence of the momentum equations:

$$\frac{\partial \delta}{\partial t} + \underbrace{\mathbf{u} \cdot \nabla \delta + \frac{\sigma^2 - \zeta^2}{2}}_{\text{ageostrophic balance}} + \underbrace{\frac{\delta^2}{2} - f\zeta}_{\text{geostrophic balance}} = -\nabla^2 P. \quad (5)$$

The first four terms in Eq. (5) ($\partial\delta/\partial t + \mathbf{u} \cdot \nabla \delta + \delta^2/2 + (\sigma^2 - \zeta^2)/2$) correspond to the divergence of the Lagrangian accelerations, the fifth term ($-f\zeta$) to the divergence of the Coriolis forces, and the last term to the divergence of pressure gradients ($-\nabla^2 P$). When the divergence of the Lagrangian accelerations has a magnitude similar to the divergence of the Coriolis forces, the dynamical balance is not geostrophic. It is called an ageostrophic balance^{25,41}.

Terms in Eq. (5) have been computed from DopplerScatt velocities except for the last term which is treated as a residual term. The first term, the divergence tendency, is estimated from the change in divergence between the two panels of Fig. 3. DopplerScatt observations indicate that the Eulerian time derivative of the divergence, the first term in Eq. (5), is smaller than the other terms on the left-hand side. The smallness of the divergence tendency, $\partial\delta/\partial t$, compared with the nonlinear terms, in particular, the third and fourth terms in Eq. (5), strongly suggests that internal gravity waves, usually explained by linear dynamics⁴⁰, have a very weak impact on the velocity field analyzed in this study.

We have assessed the accuracy of closing the budget in eq. (5) by testing the budget vorticity equation using the two DopplerScatt flights on

October 26.

$$\frac{\partial \zeta}{\partial t} + \mathbf{u} \cdot \nabla \zeta + (f + \zeta) \cdot \delta = 0 \tag{6}$$

The budget is nonzero, but note that the budget were computed using the two flights separated by 6 h. Closing the budget is challenging since submesoscale evolved in less than 6 h. In order to estimate an error in the vorticity budget equation, the stretching term was used as reference to define relative error. Fig. 19S shows the relative error of smoothed vorticity budget equation. The relative error as a function of spatial smoothing revealed that the smallest relative error is between 2 km and 5 km. And the error accounts for 10% f_o^2 .

Eddy interactions driven by strain, vorticity, divergence, and Okubo–Weiss quantity. Dispersion of particles

One approach to diagnosing the dynamical properties of a turbulent flow in terms of eddy interactions is to analyze the dispersion of particles²⁸. If $\delta \mathbf{X}$ is the separation distance between two particles, its time evolution is given by ref. 29:

$$\frac{d}{dt} \delta \mathbf{X} = \frac{1}{2} \begin{bmatrix} \delta + \sigma_n & \sigma_s - \zeta \\ \sigma_s + \zeta & \delta - \sigma_n \end{bmatrix} \delta \mathbf{X}, \tag{7}$$

where σ_n and σ_s are respectively the normal and shear strains defined as $\sigma_n = u_x - v_y$, and $\sigma_s = v_x + u_y$, ζ is the vorticity defined as $\zeta = v_x - u_y$ and $\delta = u_x + v_y$ is the divergence. The total strain is $\sigma = \sqrt{\sigma_n^2 + \sigma_s^2}$. Then, a solution of eq. (7) is:

$$\delta \mathbf{X}(t) \approx \delta \mathbf{X}(0) \cdot e^{t \cdot (\delta \pm Q^{1/2})/2}, \tag{8}$$

with Q the Okubo–Weiss quantity defined as:

$$Q = \sigma^2 - \zeta^2. \tag{9}$$

Q quantifies the competition between strain and vorticity. When $Q > 0$, Eq. (8) indicates an exponential growth or decay of $\delta \mathbf{X}$ since strain dominates: particles diverge, or are dispersed in one direction and converge in the other direction. When $Q < 0$ is negative, vorticity dominates and therefore there is no growth or decay of $\delta \mathbf{X}$, just a rotation the particles since $Q^{1/2}$ is purely imaginary. Eq. (8) also emphasizes the direct contribution of the divergence. Thus, if the divergence is negative, particles converge.

From DopplerScatt observations, the RMS values of Q and δ are respectively f^2 and $0.69f$. Using $|Q|^{-1/2} \approx f^{-1}$ (with $f = 0.8 \times 10^{-4} \text{ s}^{-1}$), this leads to a time scale of about 3 h. From eq. (8), we can infer the particle dispersion due to the submesoscale turbulent field: the separation distance between two particles, roughly given by $\delta \mathbf{X}(t) \approx \delta \mathbf{X}(0) \cdot \exp[\pm Q^{1/2} \cdot t]$ ³⁰, increases from 1 km up to 50 km in 12 h. The same increase will take more than 20 days if only the mesoscale eddy field is present (for which $|Q|^{1/2} < 0.05f$), which highlights the strong impact of submesoscale turbulence on the 2-D dispersion.

Kinetic energy fluxes across scales

The scale kinetic energy flux ($\Pi(L)$) is the rate of transfer of kinetic energy between scales larger than a specific horizontal scale L and scales smaller than L ³². The coarse-graining approach is used to estimate the fluxes³¹. This method has been widely used to investigate kinetic energy fluxes between mesoscale eddies and scales between 1 km and 50 km³².

The method relies on a low-pass filter through a convolution $\bar{F}(x, y) = C \times F(x, y)$ with a top-hat kernel

$$C(\mathbf{r}) = \begin{cases} 1/A, & \text{if } |\mathbf{r}| < L/2. \\ 0, & \text{otherwise.} \end{cases} \tag{10}$$

where $A = \pi L^2/4$ is the circular normalization area of diameter L and \mathbf{r} is the radial position vector.

We employed the same filter here as in the literature to be able to compare the magnitude of the fluxes. These fluxes are given by (see refs. 31,32 for the derivation):

$$\Pi(L) = (\overline{u'^2} - \overline{v'^2}) \frac{\overline{\sigma'_n}}{2} - \overline{u'v'} \overline{\sigma'_s} - (\overline{u'^2} + \overline{v'^2}) \frac{\overline{\delta}}{2}, \tag{11}$$

where prime (overline) velocities are obtained using a high-pass (low-pass) filter using L as a threshold. The computation of Π was performed in a regular grid with 200 m grid spacing using DopplerScatt velocities without previous smoothing to avoid confusion. We have chosen $L = 5$ km.

Negative values of Π are associated with upscale kinetic energy flux (from smaller scales to larger scales relative to L) and positive values with downscale (from larger scales to smaller scales relative to L). Estimation of Π using DopplerScatt data revealed that the terms related to strain, σ_n and σ_s , have the same order of magnitude as the term related to divergence, δ . The term related to divergence emphasizes that the time scale associated with kinetic energy ($u'^2 + v'^2$), is the divergence time scale, i.e., a few hours. This is consistent with the fast-time evolution of the submesoscale eddy field.

Data availability

Data of DopplerScatt for the S-MODE experiment can be download through PO.DAAC data portal: [DopplerScatt dataset](#). A closer look of the data used in this manuscript can be found at: [S-MODE-closer-look](#).

Code availability

Code and examples, along with video explanations for working with DopplerScatt data are available from PO.DAAC's GitHub page, [S-MODE GitHub](#).

Received: 4 June 2024; Accepted: 18 November 2024; Published online: 19 December 2024

References

1. Munk, W., Armi, L., Fischer, K. & Zachariasen, F. Spirals on the sea. *Proc. R. Soc. Lond. Ser. A Math. Phys. Eng. Sci.* **456**, 1217–1280 (2000).
2. Ni, Q., Zhai, X., Wilson, C., Chen, C. & Chen, D. Submesoscale eddies in the south china sea. *Geophys. Res. Lett.* **48**, e2020GL019555 (2021).
3. Shcherbina, A. Y. et al. Statistics of vertical vorticity, divergence, and strain in a developed submesoscale turbulence field. *Geophys. Res. Lett.* **40**, 4706–4711 (2013).
4. Poje, A. C. et al. Submesoscale dispersion in the vicinity of the deepwater horizon spill. *Proc. Natl. Acad. Sci. USA* **111**, 12693–12698 (2014).
5. Thompson, A. F. et al. Open-ocean submesoscale motions: a full seasonal cycle of mixed layer instabilities from gliders. *J. Phys. Oceanogr.* **46**, 1285–1307 (2016).
6. D'Asaro, E. A. et al. Ocean convergence and the dispersion of flotsam. *Proc. Natl. Acad. Sci. USA* **115**, 1162–1167 (2018).
7. Yu, X. et al. An annual cycle of submesoscale vertical flow and restratification in the upper ocean. *J. Phys. Oceanogr.* **49**, 1439–1461 (2019).
8. Siegelman, L. et al. Enhanced upward heat transport at deep submesoscale ocean fronts. *Nat. Geosci.* **13**, 50–55 (2020).
9. Balwada, D., Xie, J.-H., Marino, R. & Feraco, F. Direct observational evidence of an oceanic dual kinetic energy cascade and its seasonality. *Sci. Adv.* **8**, eabq2566 (2022).
10. Taylor, J. R. & Thompson, A. F. Submesoscale dynamics in the upper ocean. *Annu. Rev. Fluid Mech.* **55**, 103–127 (2023).

11. Soh, H. S. & Kim, S. Y. Diagnostic characteristics of submesoscale coastal surface currents. *J. Geophys. Res. Oceans* **123**, 1838–1859 (2018).
12. Alexakis, A. et al. Large-scale self-organization in dry turbulent atmospheres. *Science* **383**, 1005–1009 (2024).
13. Freilich, M., Lenain, L. & Gille, S. T. Characterizing the role of non-linear interactions in the transition to submesoscale dynamics at a dense filament. *Geophys. Res. Lett.* **50**, e2023GL103745 (2023).
14. Rodriguez, E. On the optimal design of doppler scatterometers. *Remote Sens.* **10**, (2018). <https://www.mdpi.com/2072-4292/10/11/1765>.
15. Farrar, J. T. et al. S-mode: The sub-mesoscale ocean dynamics experiment. In *Proc. IGARSS 2020 IEEE International Geoscience and Remote Sensing Symposium*, 3533–3536 (IEEE, 2020).
16. Rudnick, D. L. On the skewness of vorticity in the upper ocean. *Geophys. Res. Lett.* **28**, 2045–2048 (2001).
17. Buckingham, C. E. et al. Seasonality of submesoscale flows in the ocean surface boundary layer. *Geophys. Res. Lett.* **43**, 2118–2126 (2016).
18. Torres, H. S. et al. Separating energetic internal gravity waves and small-scale frontal dynamics. *Geophys. Res. Lett.* **49**, e2021GL096249 (2022).
19. Fox-Kemper, B., Ferrari, R. & Hallberg, R. Parameterization of mixed layer eddies. part I: theory and diagnosis. *J. Phys. Oceanogr.* **38**, 1145–1165 (2008).
20. Callies, J., Ferrari, R. & Bühler, O. Transition from geostrophic turbulence to inertia-gravity waves in the atmospheric energy spectrum. *Proc. Natl. Acad. Sci. USA* **111**, 17033–17038 (2014).
21. Capet, X., McWilliams, J. C., Molemaker, M. J. & Shchepetkin, A. F. Mesoscale to submesoscale transition in the California Current System. part I: flow structure, eddy flux, and observational tests. *J. Phys. Oceanogr.* **38**, 29–43 (2008).
22. Klein, P. High-frequency winds and eddy-resolving models. in *Ocean Modeling in an eddying regime*, 83–100 (AGU Publications, 2008).
23. McWilliams, J. C. Submesoscale currents in the ocean. *Proc. R. Soc. A* **472**, 20160117 (2016).
24. Callies, J., Ferrari, R., Klymak, J. M. & Gula, J. Seasonality in submesoscale turbulence. *Nat. Commun.* **6**, 1–8 (2015).
25. Capet, X., McWilliams, J. C., Molemaker, M. J. & Shchepetkin, A. F. Mesoscale to submesoscale transition in the California current system. part III: energy balance and flux. *J. Phys. Oceanogr.* **38**, 2256–2269 (2008).
26. Shakespeare, C. J. Curved density fronts: cyclogeostrophic adjustment and frontogenesis. *J. Phys. Oceanogr.* **46**, 3193–3207 (2016).
27. Hua, B. L. Skewness of the generalized centrifugal force divergence for a joint normal distribution of strain and vorticity components. *Phys. Fluids* **6**, 3200–3202 (1994).
28. Hua, B. L., McWilliams, J. C. & Klein, P. Lagrangian accelerations in geostrophic turbulence. *J. Fluid Mech.* **366**, 87–108 (1998).
29. Okubo, A. Horizontal dispersion of floatable particles in the vicinity of velocity singularities such as convergences. in *Deep Sea Research and Oceanographic Abstracts*, Vol. 17, 445–454 (Elsevier, 1970).
30. Weiss, J. The dynamics of enstrophy transfer in two-dimensional hydrodynamics. *Phys. D Nonlinear Phenom.* **48**, 273–294 (1991).
31. Aluie, H., Hecht, M. & Vallis, G. K. Mapping the energy cascade in the north atlantic ocean: the coarse-graining approach. *J. Phys. Oceanogr.* **48**, 225–244 (2018).
32. Srinivasan, K., Barkan, R. & McWilliams, J. C. A forward energy flux at submesoscales driven by frontogenesis. *J. Phys. Oceanogr.* **53**, 287–305 (2023).
33. Marino, R., Mininni, P. D., Rosenberg, D. & Pouquet, A. Inverse cascades in rotating stratified turbulence: fast growth of large scales. *Europhys. Lett.* **102**, 44006 (2013).
34. Pouquet, A., Marino, R., Mininni, P. D. & Rosenberg, D. Dual constant-flux energy cascades to both large scales and small scales. *Phys. Fluids* **29**, 111108 (2017).
35. Hoskins, B. J. & Bretherton, F. P. Atmospheric frontogenesis models: mathematical formulation and solution. *J. Atmos. Sci.* **29**, 11–27 (1972).
36. Ballarotta, M. et al. On the resolutions of ocean altimetry maps. *Ocean Sci.* **15**, 1091–1109 (2019).
37. Rio, M.-H. et al. Improving the altimeter-derived surface currents using high-resolution sea surface temperature data: a feasibility study based on model outputs. *J. Atmos. Ocean. Technol.* **33**, 2769–2784 (2016).
38. Rodríguez, E. et al. Ka-band doppler scatterometry over a loop current eddy. *Remote Sens.* **12**, 2388 (2020).
39. Wineteer, A. et al. Measuring winds and currents with ka-band doppler scatterometry: an airborne implementation and progress towards a spaceborne mission. *Remote Sens.* **12**, 1021 (2020).
40. Vallis, G. K. *Atmospheric and oceanic fluid dynamics* (Cambridge University Press, 2017).
41. Molemaker, M. J., McWilliams, J. C. & Capet, X. Balanced and unbalanced routes to dissipation in an equilibrated Eady flow. *J. Fluid Mech.* **654**, 35–63 (2010).

Acknowledgements

This work was performed at the Jet Propulsion Laboratory, California Institute of Technology under prime contract with NASA (80NM0018D0004), and was awarded under NASA Research Announcement (NRA) NNH17ZDA001N-EVS3, Research Opportunities in Space and Earth Science (ROSES-2017), Appendix A.34: Earth Venture Suborbital-3; NASA Sub-Mesoscale Ocean Dynamics Experiment (NASA S-MODE). US government sponsorship acknowledged. PK acknowledges support from the SWOT Science Team, the NASA S-MODE project and the QuickScat mission. This study has been much inspired and motivated by the S-MODE project and the DopplerScatt instrument. The DopplerScatt team extends its gratitude to the crew of pilots and ground crew of the NASA King Air B200 aircraft for all the support during S-MODE field campaigns.

Author contributions

H.T. and P.K. led the data analysis and data interpretation. H.T., P.K., E.R., A.W., E.D., A.T., and J.C. drafted the manuscript. E.R. and A.W. processed DopplerScatt. J.T.F., E.D., and E.R. led the S-MODE experiment. D.P.-M. led DopplerScatt instrument. H.T., A.W., F.P., and R.A. were DopplerScatt operators during S-MODE experiment. All authors contributed to the scientific interpretation of the results and reviewed the manuscript.

Competing interests

The authors declare no competing interests.

Additional information

Supplementary information The online version contains supplementary material available at <https://doi.org/10.1038/s43247-024-01917-3>.

Correspondence and requests for materials should be addressed to Hector S. Torres.

Peer review information *Communications Earth & Environment* thanks Cedric Chavanne and the other, anonymous, reviewer(s) for their contribution to the peer review of this work. Primary Handling Editors: Jennifer Veitch and Alireza Bahadori. A peer review file is available

Reprints and permissions information is available at <http://www.nature.com/reprints>

Publisher's note Springer Nature remains neutral with regard to jurisdictional claims in published maps and institutional affiliations.

Open Access This article is licensed under a Creative Commons Attribution-NonCommercial-NoDerivatives 4.0 International License, which permits any non-commercial use, sharing, distribution and reproduction in any medium or format, as long as you give appropriate credit to the original author(s) and the source, provide a link to the Creative Commons licence, and indicate if you modified the licensed material. You do not have permission under this licence to share adapted material derived from this article or parts of it. The images or other third party material in this article are included in the article's Creative Commons licence, unless indicated otherwise in a credit line to the material. If material is not included in the article's Creative Commons licence and your intended use is not permitted by statutory regulation or exceeds the permitted use, you will need to obtain permission directly from the copyright holder. To view a copy of this licence, visit <http://creativecommons.org/licenses/by-nc-nd/4.0/>.

© The Author(s) 2024